An effective, economic, aspirated radiation shield for air temperature observations and its spatial gradients

CHRISTOPH K. THOMAS * AND ALEXANDER R. SMOOT

College of Earth, Ocean, and Atmospheric Sciences; Oregon State University, Corvallis, OR

ABSTRACT

We present the design and evaluate the performance of a double-walled electrically aspirated radiation shield for thermometers measuring air temperature and its gradients in the atmospheric surface layer. Tests were performed to quantify its solar radiation error, wake production, and to characterize the observer effect of the forced aspiration on vertical temperature gradients in the calm and stable boundary layer. Construction requirements were to design a unit that uses inexpensive off-the-shelf components, is easy to assemble, facilitates reconfiguration to accommodate various sensors, and reduces power consumption with the goal of reducing costs and enabling use in sensor networks in remote locations. The custom-aspirated shield was evaluated in reference to a triple-walled commercially available model and subjected to rigorous testing in a wind tunnel and field experiments.

The relative radiation error of air temperature measurements in the custom-aspirated shield was equal to or smaller than that in the reference shield within $\pm$ 0.08 K for solar irradiances $\geq$ 1000 W m^{-2} and calm winds. At night, thermal imagery revealed no significant differences in surface temperatures of both shields and the air temperature. Both shields produced significant wake within a $\pm$ 30 ° sector of incident flow. Even for weak flows $\leq$ 0.7 m s^{-1}, higher-order moments were increased by a factor of 3, while the mean airflow speed was reduced by up to 30 % compared to uncontaminated directions. Careful inspection of the spatiotemporal dynamics of air temperatures in a vertical profile showed negligible impact of the forced aspiration on the fine-scale structure of the observations for the nocturnal and transitional calm surface layers.

1. Introduction

Air temperature is of central importance to studies investigating the heat transfer in the natural and built environment including atmosphere-vegetation interactions, land and sea surface energy exchange, weather forecasting, and climate change science. The temperature of a fluid or object indexes its thermal energy, and in reference to its environment, is a measure of its ability to communicate this energy to other fluids or objects in the form of heat. Since one's ability to accurately measure air temperature and precisely determine its spatiotemporal gradients is directly related to the uncertainty of the analyses employing the air temperature observations, the design and evaluation of air temperature sensors have received much attention in the literature. For surface meteorology applications, it is customary to place the air temperature sensing element, i.e. the thermometer, in a protective enclosure to i) prevent mechanical damage by excessive momentum transfer and objects suspended in the flow during strong winds, and other external influences such as animals, ii) keep the sensor surface dry to prevent errors arising from the wet-bulb depression, iii) prevent the accumulation of particu-

late matter and development of biofilms that may change the sensor's physical properties such as diameter, time constant, and reflectivity, and iv) minimize the radiation error. As the latter typically dominates the overall measurement uncertainty except for very fine-wire sensors, the enclosures are often termed radiation shields, while they also serve the other purposes.

The basic types of radiation shields are stacked plates and concentric tubes that are either naturally ventilated or employ forced aspiration using electric fans. Naturally ventilated radiation shields are typically more economic and require no electric power for aspiration, which is beneficial for sensor networks consisting of multiple stations in remote locations. Much attention has been devoted to characterizing the airflow (**?**), radiative regime (**??**), and different coatings (**?**) on the energy balance of naturally ventilated shields which may lead to significant errors in air temperature measurements of 2 to 8 K under weak winds $\leq$ 1 m s^{-1} and high solar irradiance $\geq$ 800 W m^{-2} (e.g. **??????**). Some progress has been made to model the energy balance of naturally ventilated radiation shields with the goal of correcting for the radiation error in post-processing using concurrent measurements of wind speed and shortwave

and longwave radiative fluxes outside the radiation shield (**???**). A recent study by **?** proposed an approach that does not rely on concurrent measurements, but is based on the use of temperature sensors of different diameter to estimate the radiation error. However, significant uncertainty remains for air temperature measurements in naturally ventilated shields even after careful correction arising from i) assumptions of airflow efficiency (**?**), which is defined as the ratio between the airspeed inside the shield and wind speed outside the shield, ii) shortwave radiation penetration ratios into the shield (**?**), iii) simplifications built into shape factors representing the shield geometry (**??**), and iv) accuracy and representativeness of meteorological input variables and other assumptions such as standardized measurement height required in corrections (**?**). The latter is of particular importance for sensor networks deployed in mountainous terrain and landscapes characterized by vegetation cover of varying density and architecture such as open forests and savannas that do not allow for straightforward modeling of the radiative fluxes and wind speeds because of their large variability in wind, radiation, and thermal microclimates on scales of less than a tens or hundreds of meters (**??**). In such cases, the remaining uncertainty in air temperature measurements can amount to several tenth degrees Kelvin and thus equate to or exceed the magnitude of the spatiotemporal gradients of interest (**?**).

Although the use of radiation shields with forced aspiration avoids or significantly reduces these air temperature errors, the costs for commercially available types are prohibitive and often exceed those of the thermometer by far. This may be of particular concern for the growing number of surface meteorology micro-scale networks dedicated to studying the spatial structure of wind, air temperature and humidity, and snow (e.g. **?**, and references therein) as costs grow linearly with the number of stations. Additional concerns are associated with the need for electric power of typically 5 to 20 W per aspirated radiation shield, the sampling of greater volumes for weak winds compared to naturally ventilated shields, and the alteration of the airflow around the air intake and exhaust. The latter has been speculated to introduce an observer effect by breaking up the fine-scale structure of stably stratified flows through turbulent mixing induced by the fan (**??**).

In this study, we propose the design of an aspirated shield that addresses the concerns listed above with the intention of reducing the uncertainty in air temperature measurements and its spatiotemporal gradients by promoting the use of aspirated shields in micro-meteorological, ecological, and hydrologic micro-networks. The specific goals were to construct and evaluate a radiation shield whose a) construction is simple, fast, and uses only economic off-the-shelf components to keep costs at a minimum, b) radiation error is similar or better than those of most commercially available shields, c) design is flexible enough to accommodate a variety of sensor shapes, sizes and applications, d) impact on the flow and thermal structure of the air around the sensor is known, particularly for weak wind flows and stable stratification.

2. Theory of radiation error

The theoretical and analytical concept used to quantify the radiation error applies to both naturally ventilated and aspirated radiation shields alike. Both the thermometer and the radiation shield, like any other object, exchange energy with their environment via radiation and convection. Here, conduction through the wall of the sensor housing is assumed to be negligible because of the low thermal conductivity of its material and the small thermal gradients between where the sensor mounts to the radiation shield and the temperature sensing element. In equilibrium with its environment and assuming a dry surface, any excess or deficiency of radiative energy must be balanced by convective sensible heat exchange, so that

$$R_n + H = 0, \tag{1}$$

where R_n is the net radiation balance and H the convective sensible heat transfer. Substituting parameterizations for both terms and differentiating between shortwave, solar and longwave, terrestrial radiation yields (**??**)

$$\left(\frac{1-\overline{\rho_s}}{2}\right)\left(\frac{2K\downarrow}{\pi} + K_d + K\uparrow\right) + \frac{1}{2}\left(I\downarrow + I\uparrow - 2\epsilon_s\sigma T_s^4\right) + h\left(T_s - T_a\right) \tag{2}$$

where $\overline{\rho_s}$ is the average reflection coefficient for shortwave radiation of the surface [1], $K\downarrow$ the direct-beam and K_d the diffuse downwelling shortwave irradiance [W m^{-2}], $K\uparrow$ the reflected shortwave irradiance, $I\downarrow$ and $I\uparrow$ the down- and upwelling longwave irradiance respectively [W m^{-2}], ϵ_s the average emission coefficient for longwave radiation of the surface [1], σ the Stefan-Boltzman constant [W m^{-2} K^{-4}], h the convective heat transfer coefficient [W m^{-2} K^{-1}], T_s the surface temperature [K], and T_a the true air temperature [K]. In this general formulation of the heat budget, the subscript 's' stands for the 'surface' of interest, so either the surface of any of the concentric tubes of the radiation shield or the sensing element. A more explicit model of the sensor's heat budget would need to consider the transfer from the outer to the inner tube, from the inner tube to the sensor's protective housing, and from the protective housing to the sensing element, which is outside the scope of this study. In the case of the outermost tube of the radiation shield exposed to the environment, maximizing the reflection and emission coefficients of the exterior surface reduces R_n since a minimum amount of energy is absorbed, which must then be dissipated. The convective heat exchange depends on the wind speed of the airflow

around it, since $h \propto Nu \propto Re^m \propto U^m$ with $m \leq 0.5$ (e.g. **?**), where Nu and Re are the Nusselt and Reynolds numbers, respectively, and U is the total resultant wind speed defined as $U = (u^2 + v^2 + w^2)^{\frac{1}{2}}$, where u, v, and w are the along-, cross-, and vertical wind components. For low wind speeds and large solar heating, the heat transfer of the outermost radiation shield may approach free convective conditions which leads to $h \propto Pr_t^n$ with $n \leq 0.5$, where Pr_t is the turbulent Prandtl number (e.g. **?**). In case of the inner radiation shields or the sensor exposed to the inside of the radiation shield, the impact of short-wave radiation is minimized by careful design, i.e., $K \downarrow = K_d \approx 0$ W m^{-2}, which leaves the longwave radiative and convective heat transfers as the dominating terms. Low low emission coefficients reduce the energy transferred radiatively between the surfaces; the forced aspiration of the inside of the shield and the thermometer at an airflow rate typically ≥ 2.5 m s^{-1} maintains an efficient convective heat transport and helps eliminate temperature differences between the air, the sensor, and the inside of the shield. An statistical evaluation of the surface temperature T_s of the radiation shields is presented in Section 4a.

In summary, an air temperature measurement employing an aspirated radiation shield minimizes the radiation error by minimizing R_n and maintaining a sufficiently large h independent of environmental conditions. Air temperature measurements using naturally ventilated radiation shields can minimize the radiation error only be reducing R_n through design, while only limited control over h can be exerted by selecting a sensor with a small diameter d, since $h \propto Nu\, d^{-1} \propto Re^m\, d^{-1} \propto d^{(m-1)}$. However, designing a naturally ventilated radiation shield that minimizes R_n by reducing any K term in Eq. 2 inevitably leads to a small airflow efficiency and speed inside the shield.

3. Design

We selected a design based on a simple single-walled predecessor model made from PVC pipe (Hans-Peter Schmid, pers. comm.). The objective was to create a radiation shield whose design would require only inexpensive, easily obtainable materials. A list of materials used in the construction can be found in Table 1 with conversions from metric to imperial units given in Table 2. The construction of the custom-aspirated shield (CAS) required three steps: a) building a double-walled shield using sections of concentric PVC pipe, b) building an aspirator unit, and c) connecting the aspirator unit to the shield while allowing air to flow past the sensor at a sufficient flow rate.

a. Shield chamber

The shield construction employs two 0.153 m (6 in.) lengths of 0.042 m outer diameter (1-1/4 in. NPS) Class 200 PVC pipe and one 0.145 m (5-3/4 in.) length of 0.033

m outer diameter (1 in. NPS) Class 200 PVC pipe. NPS stands for nominal pipe size. Each length of pipe has a 45° cut at one end. The 0.033 m (1 in. NPS) pipe is secured inside one of 0.042 m (1-1/4 in. NPS) pipe lengths using wooden dowels (Fig. 1a, b). PVC cement is used to bond the two pieces of 0.042 m (1-1/4 in. NPS). PVC at their angled ends to form the 90° construction (Fig. 1b). In order to ensure a maximum surface reflection coefficient, white glossy paint is applied to the outside of the pipe construction. Finally, in order to prevent contact between the sensor and the walls of the shield and thus heat conduction, straws are glued to the inside of the inner shield to support the sensor housing (Fig. 1c).

b. Fan assembly

The source of the aspiration on the CAS design is a 0.06 m, 12 VDC fan (see Table 1), mounted to a Sched 40 PVC reduced coupling. In order to mount the coupling, it is necessary to fabricate a disk shaped mounting plate from a sheet of polycarbonate (Fig. 1d). The fan and finger guard are mounted to the mounting disk using machine screws with the wire leads fed through a hole in the plate (Fig. 1e). The mounting disk is then be fixed to the bell reducer with the fan on the inside (Fig. 1f).

c. Main assembly

The shield and fan components were joined to construct the final assembly (Fig. 1g). In order to fit the sensor securely into the 0.042 m (1-1/4 in. NPS) to 0.021 m (1/2 in. NPS) reduced bushing, the 0.021 m (1/2 in. NPS) opening was bored out with a dremel grinder. PVC cement was used to make sure all PVC fittings were secured to each other.

d. Alternative Configuration: Vertical profile variant

The design of the custom-aspirated shield was modified for the measurement of air temperature in a vertical profile using thermocouples (Fig. 1h, see Section 4c). This construction did not make use of the elbow-shaped design, instead favoring a simpler, straight horizontal sleeve geometry while retaining the double-walled shield. The sensor input needed to be plugged with duct seal to support the thermocouple housing and ensure that it did not touch the inside of the shield walls. The end of the outer sleeve was cut at a 45° angle to prevent rain entering the shield.

4. Evaluation and discussion

a. Field experiment to quantify radiation error

The field evaluation of the custom radiation shield was performed using air temperature observations over a period of approximately 20 days between May and August 2011 with the air intake installed at 2 m height above short grass

in the flat bottom lands of the Willamette Valley, OR. Data from individual periods of 3 to 5 days were combined to reflect the seasonal changes in solar irradiance and azimuth, surface reflection coefficient as the grass senesces, wind speed, and precipitation. Air temperature measurements were collected using a combined probe (Model HMP-155A, platinum-wire Pt-100, Vaisala, Helsinki, Finland, the successor to the popular Model HMP45C) placed in 4 different radiation shields: a commercially available triple-walled aspirated shield (Model 43502, RM Young, Traverse City, MI, USA, see Table 3) used as a reference, hereafter referred to as as REF, and three identical double-walled custom-aspirated shields (CAS, see Table 3) with the intake pointing in three different directions, north, east, and south, hereafter referred to as CAS-N, CAS-E, and CAS-S, respectively. The analog output voltages for air temperature and humidity were recorded using the analog input channels of a sonic anemometer (Model 81000VRE, RM Young, Traverse City, MI, USA) at a sampling rate of 10 Hz, digitized using the on-board 12-bit AD converter, and sent as binary serial string to a data logger (Model Cr3000, Campbell Scientific Inc., Logan, UT, USA) for storage. The measurement resolution of the described sampling and data acquisition system was 0.04 K. The oversampled signals were aggregated to 1 min averages during post-processing, which corresponds to approximately 2 to 3 times the time constant of the sensor specified as $\approx$ 20 to 30 s according to the manual. Note that for the purpose of this study, the sintered PTFE filter protecting the sensing elements was not considered an additional radiation shield when evaluating the radiation error of the aspirated shields. This simplification is justified since the sensor and its housing used in the different radiation shields was identical, and our objective was to construct a inexpensive radiation shield that performs equally or better than commercially available models, and not to comprehensively evaluate the heat budget of the sensor. To account for any systematic biases in air temperature measurements between the sensors in the different radiation shields, a linear regression model was applied to all observations in CAS. Model coefficients were determined using all nighttime data with wind speeds $U \geq 1 \, \mathrm{m \, s^{-1}}$ when radiation errors and differences between radiation shields are assumed to equal zero. This assumption was verified by measuring the brightness surface temperature of the radiation shields, i.e., the emitted infrared radiation, including the air intake using a thermal infrared camera (Model SC305, FLIR, Wilsonville, OR, USA) as a function of the downwelling shortwave irradiance (Fig. 2). Raw measurements from the camera were corrected for the body temperature of the external optics, the air temperature and humidity between the camera and the radiation shields, the emissivities of the radiation shields, and reflected surrounding objects. At night when $K \downarrow \approx 0$ W m^{-2}, the surface temperature of the innermost radiation

shield of both the custom-aspirated and reference shields was equal to the air temperature measured by the thermometers for wind speeds $U \approx 1 \, \mathrm{m \, s^{-1}}$. Downwelling shortwave irradiance was measured using a pyranometer (Model PSP, The Eppley Laboratory Inc., Newport, RI, USA) averaged over 1 min increments. Since the objective was to design a radiation shield with an equal or higher efficiency than that of a commercially available reference shield, the relative difference $\Delta T = (T_{CAS} - T_{REF})$ will be used to evaluate the radiation error as a function of shortwave downwelling irradiance and total wind speed according to Eq. 2, where T_{REF} and T_{CAS} are the air temperatures measured inside the reference and custom shields respectively.

In general, the magnitude of the relative radiation error was very small with $|\Delta T| \leq 0.12$ K (Fig. 3), which corresponds to 3 times the physical measurement resolution and effective uncertainty of the air temperature measurement, $\sigma_{\Delta T}$. The latter is the precision of the measurement setup and was defined as the standard deviation of the temperature differences between air temperature observations in REF and CAS for all nighttime data exceeding $U \geq 1$ m s^{-1} after application of the linear correction model mentioned above determined at $\sigma_{\Delta T}$=0.04 K. Some behaviour, however, was systematic albeit its small magnitude and significant scatter. The relative radiation error ΔT was insensitive to the orientation of the CAS for irradiances $K \downarrow \leq 500$ W m^{-2} independent of wind speed. For $K \downarrow >$ 500 W m^{-2} and the south-facing CAS, $\Delta T \geq 0$ K and increased with increasing irradiance and decreasing wind speed (Fig. 3c) indicating an equal or higher radiation error for the CAS compared to that of REF. For highest irradiances and weakest flows, $\Delta T \approx 0.08$ K or $+2\sigma_{\Delta T}$ for CAS-S. The surface temperature of the innermost radiation shield at the air intake measured with the thermal infrared camera was slightly lower for REF than for CAS (Fig. 2b) by about 0.3 K, which supports the finding of the greater radiation error of CAS for this configuration. A direct experimental evaluation of the brightness surface temperature of the temperature sensing element and comparison with the measured air temperature could not be performed because of the shield design, which intentionally obstructs the direct view on to the sensor to minimize the amount of shortwave radiation entering the radiation shield. In contrast, $\Delta T \leq 0$ K and decreased with increasing wind speeds and irradiances in case of the north- and east- facing CAS, which indicates an equal or greater efficiency of the CAS compared to REF. Here, efficiency is defined as a shield's ability to minimize the solar radiation error by design and orientation.

The increase in relative radiation error for weaker winds and the south-facing CAS can qualitatively be explained by the increased amount of energy absorbed by the single-walled intake of the CAS exposed almost perpendicular to

the sun beams, as $K \downarrow$ has an angular dependence given by the cosine law, and a decrease of the convective heat transfer coefficient on the exterior surface of the shield. Both effects act to increase ΔT according to Eq. 2. In contrast, the decreased relative efficiency of REF with wind speeds ≥ 2 m s^{-2} compared to the east- and north-facing CAS is counter-intuitive and requires further investigation. One possible explanation is the orientation of the CAS relative to the wind direction which, for a specific geometry, may further increase h and thus decrease ΔT enhancing the efficiency of the CAS beyond that of REF. Stronger winds were oriented primarily perpendicular to the north-facing CAS maximizing the surface area exposed to the wind and thus h, which results in $\Delta T \approx - 0.08$ K or $-2\sigma_{\Delta T}$. This conclusion was supported by the wake analysis in the wind tunnel presented in the next section. The design of the REF shield is omnidirectional and thus the radiation error is not expected to show any dependence on the direction of the flow.

b. Wind tunnel experiment to quantify wake production

Studies investigating the atmospheric heat transport often require closely collocating wind and air temperature sensors to simultaneously observe the spatiotemporal dynamics of the flow and scalar fields, such as estimating spatial gradients, perturbations, and advection. If time scales on the order of minutes, i.e. larger than those of turbulence, are of primary interest, this is often accomplished by pairing sonic anemometers and thermometers with time constants on the order of tens of seconds housed in radiation shields. Such a setup requires careful evaluation since the radiation shield may induce significant wake affecting the flow statistics when installed in close proximity to the anemometer. However, stratified flows with small-scale motions prevalent in stable and weak-wind boundary layers, e.g. flows over ice, snow, and vegetated surfaces without significant mesoscale forcing, require both sensors to be mounted at the same height and at a small horizontal separation distance to physically sample the same air volume. For evaluation of the impact, one sonic anemometer in combination with a thermo-hygrometer housed in a reference shield, REF, and one using a custom-aspirated shield, CAS, were placed side-by-side at the end of the 10 m free-stream section of a wind tunnel with a cross section of 1.5 m by 1.5 m (Fig. 4). The sampling protocol was identical to that described in the previous section. The onboard head correction reducing the effect of the flow distortion introduced by the support struts was enabled. The center of the sonic anemometer paths was vertically aligned with the air intake of the radiation shields at 0.8 m above the tunnel floor and horizontally separated by 0.35 m. The sensors were mounted on a rotating baseplate to facilitate adjusting their orientation relative to the incident flow. Statistics were computed using the recorded 10 Hz

samples over a 3 min period for the position of $\pm 45°$, $\pm 30°$, $\pm 15°$, $\pm 7.5°$, and $0°$ at the airflow speeds of 0.7, 1.5, 3.4, and 6 m s^{-1}. The position of $0°$ refers to a configuration when the along-wind component of the airflow, the radiation shield, and the sonic anemometer are aligned (see configuration in Fig. 4). Since the CAS has a directional design, two different spatial configurations were tested: In the tangential configuration, the center line of the radiation shield was perpendicular to the line extending from the center to the support struts of the sonic anemometer when viewed from above, while both were exactly aligned in case of the radial configuration.

In general, the presence of the radiation shields significantly affected the flow statistics computed from the sonic anemometer data irrespective of airflow speed, CAS configuration, and type of radiation shield. The magnitude of the artifacts introduced by the radiation shields was proportional to the magnitude of the airflow speed in a non-linear fashion yielding the greatest relative increase from 0.7 to 1.5 m s^{-1}. Significant differences were found between REF and CAS, and between the tangential and radial CAS configuration. From this point onward, we will present results for the radial CAS configuration only since the tangential configuration led to much greater wake production as expected. The magnitude of the total resultant wind vector U was reduced by up to 19 and 28 % for the CAS and REF shields respectively (Fig. 5 a,b). **?** found similar results studying the flow distortion caused by the transducers and struts alone of a different type of sonic anemometer, but similar geometry compared to that used in this study. The higher order flow moments such as the velocity variances and the friction velocity were increased by a factor of up to 13 and 10 for the CAS and REF shields respectively (Fig. 5 c,d). Minimum ratios of σ_w were observed for the lowest airflow speeds at 0.65 and 0.54 for CAS and REF, respectively (Fig. 5b). In comparison with related studies on the effect of flow obstacles such as support and tower elements on flow statistics from sonic anemometers (**???**), the effect of the radiation shields is much larger than those caused by the support struts and transducers alone. The control run yielding the flow statistics recorded from the sonic anemometer without the presence of radiation shields yielded an increase of the velocity variances of up to a factor of 2 for an attack angle of $0°$, i.e., with the flow going through the support strut despite the enabled head correction implemented by the manufacturer, while the magnitude of the mean flow speed was unaffected. The sector of the attack angles parallel to the flow in which statistics were contaminated was relatively narrow within $\pm 30°$ for both radiation shields, which is in good agreement with similar studies (e.g. **?**).

c. Field experiment to assess impact on vertical potential temperature gradients

The aspiration of the radiation shields leads to sampling of greater air volumes compared to naturally-ventilated shields particularly when the ambient flow is weak and stratified such in dense canopies or stable boundary layers, and to an alteration of the airflow around the air intake and exhaust. **?** therefore recommended the use of naturally-ventilated shields to minimize the observer effect when making observations in these conditions. **?** compared air temperature observations from naturally-ventilated and mechanically-aspirated thermocouples in weak air flows with a significant vertical temperature gradient and concluded that the well-mixed air volume sampled with the mechanical aspiration lacks the fine-scale structure caused by slight fluctuations in streamlines on the order of 0.05 to 0.10 m. To evaluate the impact of the mechanical aspiration on measuring vertical air temperature gradients and its temporal dynamics, air temperature observations from 12 fine-wire thermocouples (Model TMTSS-020, sheath diameter $5\text{x}10^{-4}$ m, Omega Engineering Inc, Stamford, CT, USA) were analyzed. The thermocouples were housed in custom-aspirated shields oriented north-south and installed in a vertical profile at a height of 0.05, 0.10, 0.20, 0.40, 0.80, 1.50, 3.0, 4.0, 6.0, 8.0, 10.0, and 12.0 m above ground level (agl) over short grass. The thermocouples were interrogated every 2 s using a multiplexer (Model AM25T connected to a data logger Model Cr1000, both Campbell Scientific Inc., Logan, UT, USA) over the period 30 August until 01 October 2011. As a reference, a sonic anemometer was placed at a distance of $\approx$ 2 m to the east of the thermocouple profile and thus perpendicular to the predominant flow with its center of the transducers located at 0.8 m agl. The design of the custom-aspirated shields was slightly modified such that the double-walled section holding the thermocouple in its center was pointing horizontally to the north with a very short single-walled horizontal drip shield. Because of the close proximity of the lowest three sensors to the surface ground, their aspirating units exhausted horizontally to the south instead of downward. Ensemble averaged profiles of potential temperature θ were constructed for two different incident wind direction sectors, light regimes, and wind speed classes (Fig. 6). At night during weak winds and dynamically stable stratification with bulk Richardson numbers $Ri_b \geq 1$ when observer effects arising from the mechanical aspiration are expected to be large, the vertical profile of θ resembled the expected logarithmic shape typical of stable boundary layers characterized by a downward transport of sensible heat. The presence of a stationary shallow cold-air pool, which is often observed at this experimental site (**?**), led to a change in $\partial\theta \ \partial lnz^{-1}$ at its interface to the warmer overlying air at a height of approximately 1.5 m agl for $U \leq 0.6$ m s^{-1}. The behavior of the temperature observed with the lowest

sensor in relation to the rest of the profile was sensitive to the incident wind direction: for north-easterly flows when the flow was unobstructed and thus not expected to be altered by the aspirator, the mean minimum temperature was observed at 0.05 m and fit well into the logarithmic profile (Fig. 6a). For southerly flows, however, when the sample volume was potentially perturbed by the mechanical aspirator, the minimum temperature was observed at 0.10 m agl (Fig. 6b). It remains unclear if this anomaly indicates an observer effect caused by the aspiration or a physical signal, as the forced mixing induced by the fans upstream of the thermocouples would act toward eliminating any vertical temperature gradients. During the morning transition characterized by very weak winds $U \leq 0.2$ m s^{-1} but significant solar irradiance resulting in $Ri_b \leq$ -0.3, the temperature profiles resolved the vertical divergence in sensible heat flux showing a surface heating and upward heat transport close to the ground, but a downward heat transport aloft (Fig. 6c, d). Time series plots of temperature records from the thermocouples and the sonic anemometer revealed a richness in structures across the lower part of the profile for $z \leq 1.5$ m agl visible as fast-changing spatiotemporal gradients (Fig. 7). In spite of the mechanical aspiration, significant vertical differences and temporal dynamics in traces of potential temperature were conserved even for closely co-located sensors closest to the ground can be distinguished. Fine details such as a temporary reversal of the vertical temperature gradient between the lowest observation heights of 0.05 and 0.10 m agl (19:25 PST) were observed. The comparison of the dynamics of the potential temperature from the thermocouple in the custom-aspirated shield and the speed-of-sound based temperature from the sonic anemometer at the same height yielded no significant differences in first- and higher-order moments for flows perpendicular to the horizontal separation, which is in contrast with the findings by **?**. Despite the significant horizontal separation of $\approx$ 2 m, the signature of transient motions, e.g., passing at 19:26:30 PST, was registered by both sensors in a very similar fashion, which supports the finding that the aspiration does not significantly perturb the structure of the airflow and its scalar fields.

5. Conclusions

The evaluation of the double-walled custom-aspirated radiation shield led to the following conclusions with respect to the goals of the study listed in the introduction.

- The use of commercially available off-the-shelf irrigation PVC pipe, connectors, and motorized fan reduced the cost per aspirated radiation shield well below a tenth of that of an equivalent commercially available radiation shield. The variety of PVC connectors and pipes allows for easy and inexpensive ad-

justment of the shield's design to accommodate specific measurement configurations and sensors, such as the vertical profiling described in Section 4c. Particularly when many units are made at the same time, the production time can be reduced to about 20 min per unit and manufacturing can be done with simple hand tools such as cutters, power drill, screw driver, and PVC cement. The electric fan used in our design requires less power than commercially radiation shields, which is important for battery-buffered systems relying on solar power for remote applications.

- In spite of the use of inexpensive components, the radiation error for air temperature measurements in the double-walled custom-aspirated shield was less or equal to that in a triple-walled commercially available shield. Note that for the purpose of this study that aims at devising a practical, economic pathway of reducing the uncertainty in air temperature measurements over existing techniques we chose a relative measure of the radiation error in comparison with a commercially available product with a known radiation error (0.2 K at 1000 W m^{-2}, see Table 3). While this comparative approach allows constraining the radiation error of the custom-aspirated shield to < 0.2 K, the true air temperature and thus the absolute radiation error of the custom-aspirated shield ultimately remains unknown due to the inherent difficulties modeling and measuring air temperature irrespective of the approach.

- The directional design of the custom radiation shield requires the air intake pointing north to achieve a maximum efficiency and reduction of the radiation error.

- The turbulent wake induced by the custom and commercially available aspirated radiation shields is significant and needs to be considered when flow statistics are recorded with a fast response sensor such as a sonic anemometer in close proximity. The radiation shields reduce the mean speed of the flow, but inflate high-order statistics such as velocity variances and momentum transport by up to a factor of 20 compared to unobstructed incident flow directions. The sector of contaminated incident attack angles parallel to the flow is relatively narrow within $\pm$ 30 °. Even for weak flows with $U \leq 0.7$ m s^{-1}, data from these sectors need to be excluded from analysis.

- The mechanically-forced aspiration had a negligible impact on the spatiotemporal dynamics of air temperature observations and its gradients even under conditions of weak flows and stable stratification. In spite of the greater sampling volume, differences in

variety of motions on time scales on the order of seconds to tens of seconds were resolved with two sensors physically located within 0.05 m of each other close to the ground. Nighttime vertical profiles of potential temperature obeyed logarithmic scaling even for weakest flows with $U \leq 0.2$ m s^{-1} and strongly dynamic stability with $Ri_b \geq 1$.

TABLE 1. Part list for custom-aspirated shield construction. See Table 2 for conversion of Nominal Pipe Size (NPS) into metric units. PVC fittings are Schedule 40. PVC pipe and fittings can be purchased from plumbing or irrigation suppliers.

No.	Description	Quantity	Manufacturer	Cost (USD)
1	1 in. NPS Class 200 PVC Pipe	1 m	Ridgeline Pipe	1.99/3 m
2	1-1/4 in. NPS Class 200 PVC Pipe	0.3 m	Ridgeline Pipe	3.79/3 m
3	1-1/4 in. NPS PVC 45° Wye	1		6.87
4	1-1/4 in. to 1/2 in. NPS PVC reduced bushing	1		1.41
5	1-1/4 in. to 1 in. NPS PVC reduced bushing	1		1.48
6	1-1/2 in. to 1 in. NPS PVC reduced bushing	1		6.52
7	3 in. to 1-1/2 in. NPS PVC bell reducer	1		
8	0.0024 m thick (3/32 in.) polycarbonate sheet	1		7.75/sheet
9	12 VDC Fan 0.060 m x 0.025 m, Model #: 622HH	1	ebm-papst	22.55
10	0.0016 m (0.063 in.) dia. Welded Finger Guard	1	ebm-papst	3.38
11	0.05 x 0.0064 m (2 in. x 1/4 in.) dowel	6		< 1.00
12	machine screw + nut	4		5.26/100
13	wood screw	4		1.21/10
14	0.15 m (6 in.) plastic drinking straw	2		< 1.00
			Total	≈ 50.00

TABLE 2. Specifications for all types of PVC pipe used in the construction of the custom-aspirated shield. NPS stands for nominal pipe size.

NPS	Category	Outer Diameter mm [in.]	Inner Diameter mm [in.]
1/2	Sched 40	21.34 (0.840)	15.79 (0.62)
3/4	Class 200	26.67 (1.050)	23.37 (0.92)
1	Class 200	33.40 (1.315)	29.97 (1.18)
1-1/4	Class 200	42.16 (1.660)	37.85 (1.49)
1	Sched 40	33.40 (1.315)	26.16 (1.03)
1-1/4	Sched 40	42.16 (1.660)	34.54 (1.36)

TABLE 3. Specifications of commercially available and the custom-aspirated radiation shields. Met One Models 076B-1 and 076B-11 require AC power, all others use DC power. The flow rate range for the custom-aspirated shield (CAS) applies to a voltage range of 12 to 18 VDC. An image of the CAS is contained in Figure 1g. Radiation error for commercially available shields as indicated in the user manual.

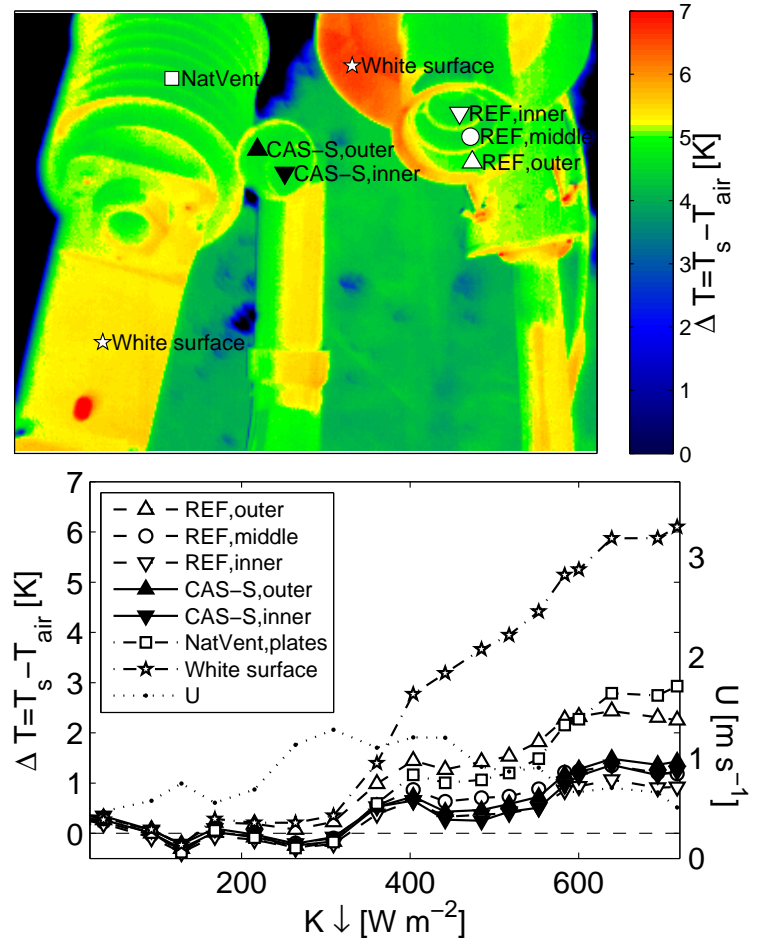| Manufacturer and Model	Shielding	Power draw [W]	Flow Ra...
RM Young 43502	Triple	6 - 7	5 -
Met One 076B-1	Double	20 (AC)	2.5
Met One 076B-4	Double	3	2.5
Met One 076B-11	Double	18 (AC)	2.5
CAS	Double	2.3	7 -

FIG. 2. Surface temperature of the radiation shields: a) Picture of the difference ΔT between brightness temperature, T_s, recorded with a thermal infrared camera and air temperature, T_{air}, observed with the sensors described in Section 4a; b) ΔT extracted for several regions of interest centered around the indicated markers and total wind speed, U, as a function of downwelling shortwave irradiance, $K\downarrow$, recorded over a 8 hour period. CAS is the double-walled custom-aspirated radiation shield described in Section 3, REF is the triple-walled reference shield described in Table 3. For comparison, a multi-plated naturally ventilated shield (NatVent, Model 41003, RM Young, Traverse City, MI, USA) was included. Images were taken with a camera looking upward into the radiation shields at an inclination angle of ≈ 45 °.
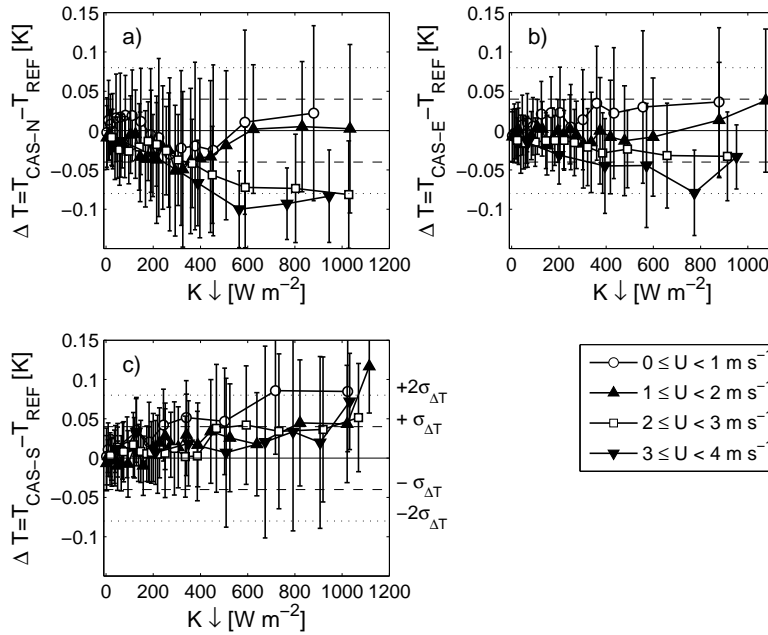

FIG. 1. Double-walled custom-aspirated radiation (CAS) shield used in this study: a) Shield wall configuration before securing with dowels; b) Shield assembly after cementing 45° edges, also shows how dowels are used to secure inner shield wall; c) Inside of the double shield, note the straws glued to the inside of the walls to separate the sensor housing from the inner wall; d) Components needed for fan assembly; e) Fan attached to mounting plate; f) Completed fan assembly; g) Completed CAS construction with sensor; h) Variant used for vertical profiling of air temperature using thermocouples (See section 4c). All numbered annotations apply to Table 1.

9

Fig. 3. Daytime relative radiation error ΔT defined as the difference between air temperature observations in the aspirated reference shield, T_{REF}, and those in the custom-aspirated shield with the air intake facing a) north, T_{CAS-N}, b) east, T_{CAS-E}, and c) south, T_{CAS-S}, as a function of downwelling shortwave irradiance, $K\downarrow$, and total wind speed, U. The one minute observations were aggregated into bins of equal number of data ($N = 150$). The vertical bars represent the standard deviation of observations within each bin. Also shown are multiples of the effective uncertainty or precision of the air temperature measurement, $\sigma_{\Delta T}$, for orientation purposes.
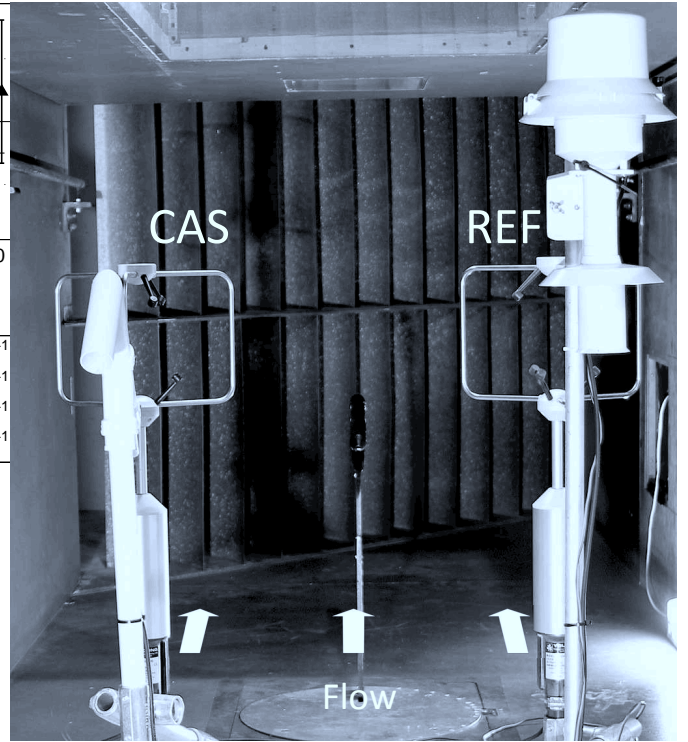
Fig. 4. Picture of the wind tunnel setup to evaluate the wake production of the custom-aspirated (CAS) and reference (REF) radiation shields on flow statistics measured with sonic anemometers. The intake of the radiation shields was separated horizontally from the center of the sonic anemometers paths by 0.35 m. The flow was directed into the image. The picture shows the configuration for an incident flow angle of 0°.
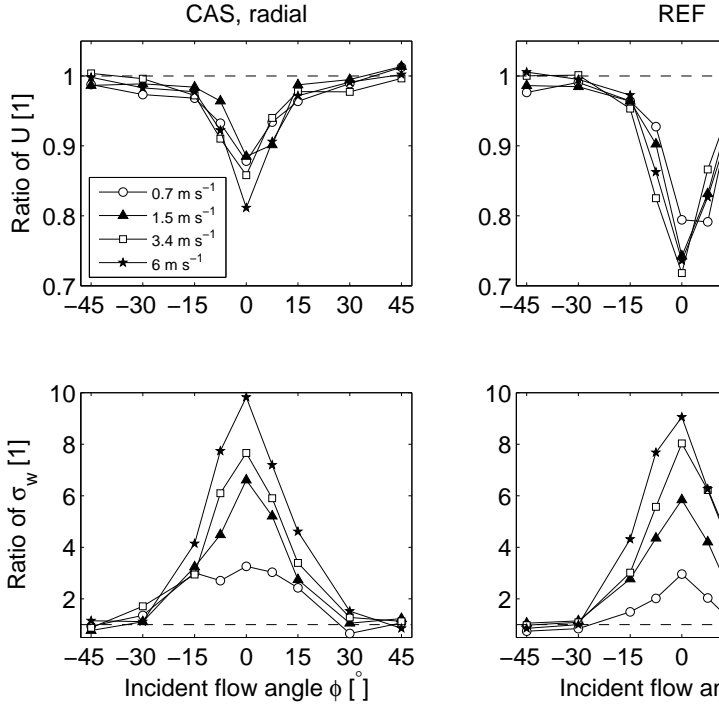
FIG. 5. Ratios of total resultant wind speed $U = (u^2 + v^2 + w^2)^{\frac{1}{2}}$ (upper panel) and vertical velocity variance σ_w (lower panel) for incident flow angles $\phi = \pm\ 45°, \pm\ 30°, \pm\ 15°, \pm\ 7.5°,$ and $0°$ relative to that averaged over those for $\phi = \pm\ 45°$ for airflow speeds of 0.7, 1.5, 3.0, and 6 m s^{-1} in the wind tunnel for the custom-aspirated radiation shield (CAS) in radial configuration and the reference (REF) shields. For details of the setup see Section 4b. An incident flow angle of $0°$ refers to a configuration when the along-wind component of the airflow, the radiation shield, and the sonic anemometer are aligned. The dashed line marks unity.
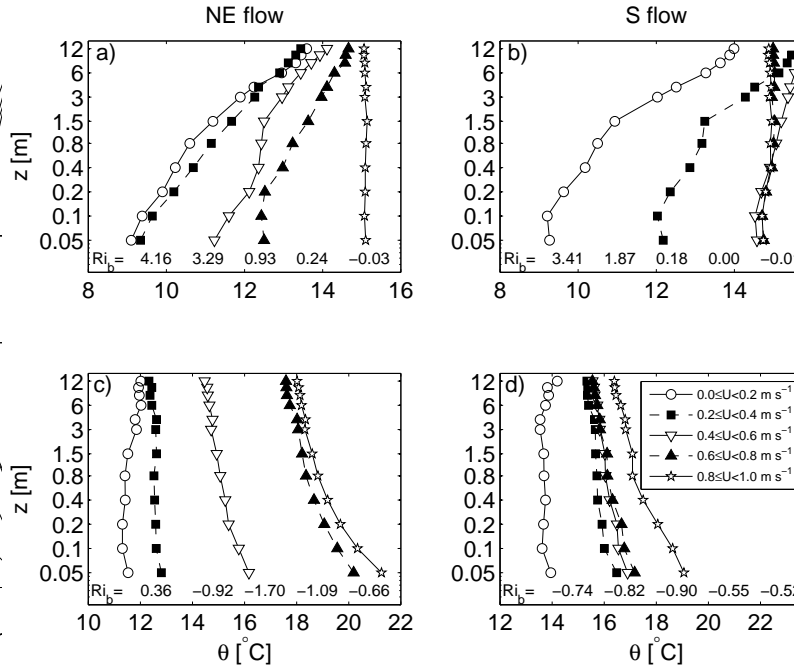
FIG. 6. Ensemble profiles of median potential temperature θ observed using thermocouples situated in the custom-aspirated radiation shields for north-easterly (NE: a, c) and southerly (S: b, d) flow for night and day and different classes of wind speeds (U) observed at 0.8 m agl. Each profile represents the median of ≥ 1000 one-minute data observed between 28 August and 01 October 2011. Also noted is the median bulk Richardson number (Ri_b) evaluated between 0.8 and 12 m agl for wind speed classes in ascending order.
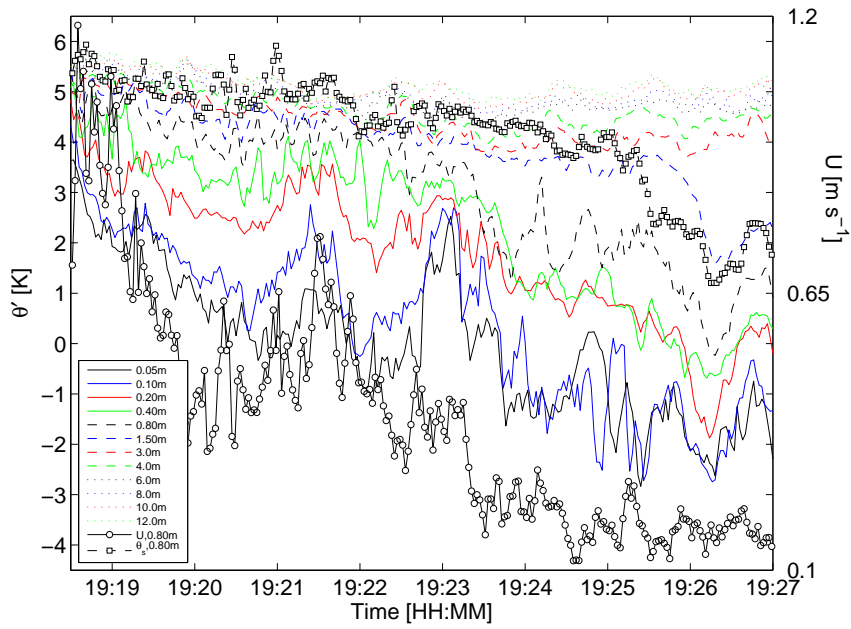
FIG. 7. Time series of potential temperature perturbations from the 30 min temporal mean measured at 0.05 m agl, θ', observed using fine-wire thermocouples situated in aspirated custom radiation shields in a vertical profile (lines) over short grass. The temporal resolution is 0.5 Hz. Also shown are the sonic potential temperature, θ_s, and the one-minute averaged total resultant wind speed, U, observed with a sonic anemometer at 0.8 m agl laterally separated from the thermocouple profile by ≈ 2 m perpendicular to the flow.